SANDIA REPORT
SAND2007-7685
Unlimited Release
Printed December 2007

Final LDRD Report: Development of Advanced UV Light Emitters and Biological Agent Detection Strategies

Mary H. Crawford, Michael A. Banas, Andrew M. Armstrong, Andrew A. Allerman, Jeffrey J. Figiel, Darcie Farrow, Randy L. Schmitt, and Darwin K. Serkland

Prepared by
Sandia National Laboratories
Albuquerque, New Mexico 87185 and Livermore, California 94550

Sandia is a multiprogram laboratory operated by Sandia Corporation,
a Lockheed Martin Company, for the United States Department of Energy's
National Nuclear Security Administration under Contract DE-AC04-94AL85000.

Issued by Sandia National Laboratories, operated for the United States Department of Energy by Sandia Corporation.

Available to DOE and DOE contractors from
U.S. Department of Energy
Office of Scientific and Technical Information
P.O. Box 62
Oak Ridge, TN 37831

Telephone: (865) 576-8401
Facsimile: (865) 576-5728
E-Mail: reports@adonis.osti.gov
Online ordering: http://www.osti.gov/bridge

Available to the public from
U.S. Department of Commerce
National Technical Information Service
5285 Port Royal Rd.
Springfield, VA 22161

Telephone: (800) 553-6847
Facsimile: (703) 605-6900
E-Mail: orders@ntis.fedworld.gov
Online order: http://www.ntis.gov/help/ordermethods.asp?loc=7-4-0#online

SAND2007-7685
Unlimited Release
Printed December 2007

Final LDRD Report: Development of Advanced UV Light Emitters and Biological Agent Detection Strategies

Mary H. Crawford, Michael A. Banas, and Andrew M. Armstrong
Semiconductor Material and Device Sciences Department

Andrew A. Allerman and Jeffrey J. Figiel
Advanced Materials Sciences Department

Darcie Farrow and Randy L. Schmitt
Laser, Optics and Remote Sensing Department

Darwin K. Serkland
RF/Optoelectronics Department

Sandia National Laboratories
P.O. Box 5800
Albuquerque, NM 87185-1086

Abstract

We present the results of a three year LDRD project which has focused on the development of novel, compact, ultraviolet solid-state sources and fluorescence-based sensing platforms that apply such devices to the sensing of biological and nuclear materials. We describe our development of 270-280 nm AlGaN-based semiconductor UV LEDs with performance suitable for evaluation in biosensor platforms as well as our development efforts towards the realization of a 340 nm AlGaN-based laser diode technology. We further review our sensor development efforts, including evaluation of the efficacy of using modulated LED excitation and phase-sensitive detection techniques for fluorescence detection of bio molecules and uranyl-containing compounds.

Acknowledgements

The authors gratefully acknowledge the technical contributions of Art Fischer, Kate Bogart, Steve Lee, David Follstaedt, Kris Fullmer and Karen Cross in the early stages of UV LED work. Steve Lee, David Follstaedt, Karen Cross and Kate Bogart also contributed to materials characterization and/or processing in support of laser development efforts. Randy Shul and Jeff Stevens provided invaluable assistance with plasma etching development for AlGaN laser diode structures and Steve Wolfley made important contributions towards the development of high reflectivity laser facet coatings. We have appreciated valuable discussions with Phil Hargis (bio material and uranium spectroscopy) and Jim Martin (frequency-domain spectroscopy techniques). Special thanks to Kathleen Holt (6772) for preparing the uranyl nitrate solutions. Finally, we have appreciated the support of managers Dan Barton (Project Manager), Bob Biefeld, Greg Hebner, and Jerry Simmons throughout this work.

Contents

Figures

Tables

1. Introduction

The ability to detect biological warfare agents with high sensitivity and a low false alarm rate is of critical importance to national security. While ultraviolet (UV)-excited fluorescence is a powerful technique for sensing of many materials, one major limitation is the lack of compact and robust light sources at the optimum UV wavelengths. A second limitation is the inability of most compact sensors to effectively discriminate against background fluorescence, and consequently such systems have unacceptably high false-alarm rates. In this LDRD project, our team sought to make significant progress in overcoming both of these limitations. In the area of UV sources, our goals included the optimization of AlGaN-based deep UV LEDs as well as the development of AlGaN-based laser diodes (LDs) to provide novel, compact, ultraviolet-emitting solid-state sources for fluorescence-based sensing applications. In concert with those efforts, we developed various fluorescence-based sensor testbed systems to evaluate sensing strategies to best take advantage of these new solid-state sources. Our efforts focused on frequency-domain techniques and phase-sensitive detection with the goal of demonstrating lifetime-selective, spectrally-resolved fluorescence measurements in a compact system. This combination of both lifetime and spectral measurements is very difficult to implement in a compact system but has clear potential to enable greater discrimination of background signatures, thus enabling reduced false alarm rates. As our program progressed, our focus expanded beyond biomaterials to evaluate nuclear materials sensing using the sensing platforms developed under this project. A final goal of the program was to assess the detection sensitivity of phase-sensitive, spectrally-resolved approaches developed under this project and to predict their potential for application to compact, fieldable sensing systems.

In the following report, we summarize the major accomplishments of this project. Section 2 describes our UV source development efforts and includes a description of efforts to optimize the performance of deep UV (270-280 nm) AlGaN-based LEDs as well as development efforts towards achieving 340 nm AlGaN LDs. Section 3 describes our sensor development efforts and includes frequency modulation characterization of the UV LED sources as well as the development and application of phase-sensitive, spectrally-resolved fluorescence measurements of both bio and nuclear simulants. Finally, section 4 presents our conclusions and suggestions for future work.

2. Development of UV Sources

Traditional UV laser-induced fluorescence (LIF) techniques use large-scale, nanosecond pulsed lasers as excitation sources. This approach to fluorescence excitation is typically combined with gated, intensified detection to maximize collection of bio-fluorescence (τ_{flu} ~13 ns) while minimizing collection of elastically scattered light and background fluorescence from common materials, including surfaces. A goal of our program was to explore the potential of applying semiconductor-based LEDs and potentially laser diodes (LDs) in combination with distinct approaches to fluorescence excitation and detection to enable a significantly more compact and flexible system with similar sensitivity and background discrimination. To be successfully

applied to our biosensor platform, new UV sources would have to meet a number of challenging performance criteria, in addition to being relatively compact. First, the devices must have peak emission at UV wavelengths of interest. Optimal wavelengths are chosen due to their strong absorption in biomaterials, and include 340 nm (strong absorption from coenzymes, including NADH) and 280 nm (strong absorption from tryptophan). Moving to shorter wavelengths, such as 250 nm, could enable increased fluorescence yield from some nuclear materials (for short-range detection schemes where atmospheric absorption is not an issue), and may therefore be of interest for sensing of such materials.

In addition to meeting these peak wavelength requirements, the UV sources should have a fairly high degree of spectral purity as the presence of defect-related emission in the blue region would interfere with fluorescence detection. Ideally, visible emission would be many orders of magnitude lower than the peak UV emission, or additional filters would be required to further reduce this emission. As described in more detail in our sensor section, the UV sources should also be compatible with modulation frequencies of at least 100 MHz to be compatible with detection of biomaterials using our modulation-based sensing approaches. This is a requirement that is fairly easily met by LDs but not so easily met by large areas LEDs. Finally, an important performance metric is the output power and ease of light collection from the UV sources, as it directly impacts the detection limits of our sensor platform. Light collection can be performed relatively efficiently from LDs, but is notably less efficient from LEDs, since emission from multiple facets of the chip results in a fairly extended source. Overall, the quantitative requirements for delivered excitation power are strongly dependent on sensor design and instrumentation, required detection sensitivity and the exact material that is being detected. One valuable outcome of our sensor development efforts, described in this report, is a determination of the sensor detection limits for particular species and at given output powers and light collection efficiencies from our UV sources.

2.1 Introduction to AlGaN-based Alloys and Light-Emitting Devices

To meet these UV source requirements, our team has focused on the development of deep UV emitters based on AlGaN semiconductor alloys. These alloys have direct energy bandgaps that can be tuned from ~365 nm (GaN) to ~200 nm (AlN), and therefore are very well suited to the deep UV wavelength requirements for bio and nuclear materials sensing. At the start of this program (October, 2004), however, AlGaN-based deep UV emitters were a very new and emerging technology. The first milliwatt-level LEDs in the < 300 nm region had just been demonstrated [1], including milliwatt-level performance at 275-300 nm by our Sandia team [2,3]. Pulsed laser diodes from GaN and AlGaN alloys had been demonstrated at 357.9 nm [4], and 350.1 nm [5], and very short-lived (seconds) pulsed lasing had been demonstrated down to 343 nm [6]. Overall, significant LED improvements were needed in the areas of output power and efficiency, spectral purity and device lifetimes. Furthermore, LDs had not yet been demonstrated at our target wavelengths (280 nm, 340 nm).

To understand our efforts to further develop and optimize AlGaN emitters, it is valuable to review the AlGaN materials properties that have frustrated their development into high performing LEDs and LDs. These alloys are part of the nitride family of semiconductors that include visible-emitting InGaN alloys that are being widely pursued for LEDs in solid state

lighting applications. Compared to InGaN LEDs, moving to higher bandgap AlGaN alloys presents a number of distinct materials challenges. First we find that doping to form both n-type and p-type material is more challenging since compensating defects are predicted to be energetically more favorable for higher bandgap alloys [7]. P-type doping is especially difficult due to extremely large acceptor activation energies which increase from ~200 meV in GaN to as high as ~400 meV in AlN materials (Mg-acceptors). A common problem for all nitride materials has been the lack of low cost, widely available native substrates [8]. Because GaN and AlGaN bulk substrates have been difficult to develop, nitride devices have commonly been grown on lattice-mismatched substrates such as SiC and sapphire, and therefore have threading dislocation densities of $5x10^8$ cm^{-2} and higher---many orders of magnitude higher than for other III-V semiconductors. Such defects are known to directly reduce operating lifetimes of LDs and may also contribute to reduced optical efficiency of both LEDs and LDs, particularly in the UV region of the spectrum.

While this substrate problem has been common to both InGaN and AlGaN devices, the nucleation of AlGaN alloys on sapphire or SiC substrates typically results in ~10X higher dislocation densities (> $1x10^{10}$ cm^{-2}) compared to GaN nucleation on these substrates (GaN templates are used in InGaN LEDs and LDs). Defect densities have been reduced by several orders of magnitude in GaN-on-sapphire templates with epitaxial lateral overgrowth (ELO) strategies which employ patterned dielectric stripes on GaN epilayers and subsequent selective area GaN regrowth to form low defect regions over the dielectric masks. The application of such approaches to achieve regions of <1e8 cm^{-2} dislocation densities was essential for the first demonstration of 10000 hr lifetimes in InGaN LDs at 405 nm [9]. Unfortunately, such ELO approaches have been problematic for AlGaN alloys due to the fact that they do not show selective area growth on dielectric masks, instead forming low quality amorphous material when deposited on SiO_2 and other dielectric mask materials. Further, the ability to form large regions of low defect density is more difficult in AlGaN due to the challenge of finding growth regimes with high ratios of lateral to vertical growth rates. A signature of the relatively high densities of extended and/or point defects in AlGaN alloys is the common presence of below bandgap emission in the near-UV and visible regions. While the origins of these defect bands are still under study, the below bandgap emission degrades the spectral purity of AlGaN LEDs and is a property that is undesirable for fluorescence-based sensing.

Whereas these materials challenges are common to both LEDs and LDs, the development of AlGaN LDs presents additional difficulties. Unlike LEDs, LDs require thicker (> 0.5 μm), transparent p-type and n-type cladding layers and this can lead to tensile strain and cracking in AlGaN-based devices. Given the difficulties in p-doping of AlGaN, developing a thick, transparent, p-type AlGaN cladding layer is clearly one of the most formidable obstacles to the demonstration of AlGaN deep UV laser diodes. In addition, the low refractive index contrast of AlGaN alloys results in relatively poor mode confinement in laser waveguide structures. Finally, LDs require more advanced fabrication processes, including the development of low-loss laser facets by either plasma etching or cleaving for cases when a compatible substrate material is used (e.g. SiC). Thus, while AlGaN-based deep UV LDs would enable greater performance in a sensor system than LEDs due to improved efficiency of light delivery, greater spectral purity, greater modulation speeds and possibly greater output powers, we find significantly more roadblocks in the path to their development.

Despite these many challenges, our team endeavored to capitalize on the opportunity that this newly emerging deep UV emitter technology presented for compact, high sensitivity fluorescence-based sensing platforms. As described below, a goal of this LDRD was to further develop the relatively immature deep UV LEDs that we had demonstrated at Sandia at the start of this project and to optimize their performance for sensing applications. In addition, we set an aggressive, "high-risk/high-payoff" goal to improve on many of the materials properties that were limiting deep UV LD demonstration with a target of demonstrating a pulsed, 340 nm AlGaN-based LD. Below we describe our efforts in each of those areas.

2.2 Deep UV AlGaN LED Optimization

The LEDs that were developed throughout this project were grown by metal-organic vapor-phase epitaxy in a VEECO D-125 reactor. Trimethylgallium (TMG), trimethylaluminum (TMA), trimethylindium (TMI) and ammonia were used as the group III and V source materials, with silane and bis(cyclopentadienyl)magnesium (Cp_2Mg) as the dopant sources. All LED structures were grown on sapphire substrates, in either on-axis (1000) c-plane orientation or 0.3° toward the m-plane. In Figure 1, we show a schematic of the design of our current generation of deep UV LEDs. AlN is used as a nucleation layer and is followed by an AlGaN buffer layer. The choice of Al composition of the buffer layer is dependent on the target wavelength of the LEDs and may be varied from 45-65% Al for emission wavelengths in the 295-270 nm range. The next layer in the structure is the Si-doped n-type AlGaN layer, which is on the order of 0.8-2 μm in thickness. The n-AlGaN layer is followed by a multi-quantum well active region with $Al_xGa_{1-x}N$ quantum wells and $Al_yGa_{1-y}N$ barriers. As a specific example, for 275 nm devices we employ three 2 nm thick $Al_{0.40}Ga_{0.60}N$ quantum wells with 5 nm thick $Al_{0.60}Ga_{0.40}N$ barriers. These compositional values are estimated from growth calibrations as well as x-ray diffraction, reflectivity and Hall

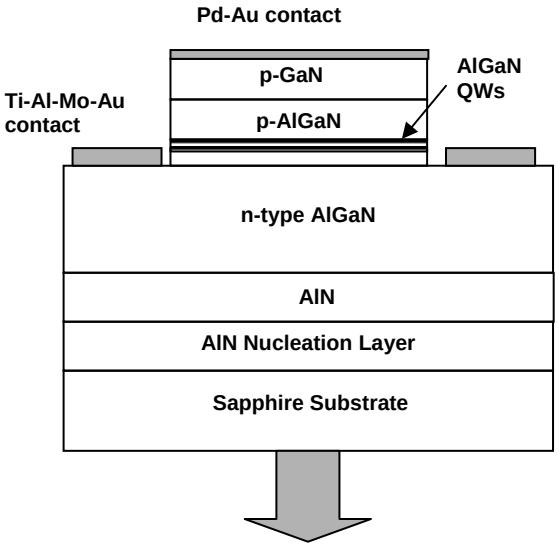

Figure 1. Schematic of AlGaN-based deep UV LED structure.

measurements of calibration structures and are estimated to be accurate to ± 1.5%. Finally, the p-type side of the LED structure is composed of an AlGaN current blocking layer with Al composition approximately 10% higher than that of the barrier material, and a thickness of 10-20 nm. The structure is completed with a 20-100 nm thick p-GaN cap layer. While this p-GaN layer is absorptive for our deep UV emission wavelength range, this loss is offset by the significantly improved metal contact resistance to p-GaN versus p-AlGaN.

Device fabrication involves standard photolithography, dry etching and metal evaporation. Mesas ranging from 200 μm x 200 μm to 1 mm x 1 mm were defined by inductively coupled plasma etching in a BCl_3/Cl_2 plasma down to the n-type AlGaN layer. Ohmic n-type contacts were formed using a Ti (15nm)/ Al (60 nm)/Mo (35nm)/ Au (50 nm) multilayer structure, and a subsequent rapid thermal anneal at 825°C for 30 seconds in N_2. The p-type contact consisted of Pd (20 nm)/Au (200nm). The completed devices were diced into arrays and flip-chip bonded to Si submounts. The submounted chips were packaged in TO-257 headers with integrated Al reflectors, as shown in Figure 2.

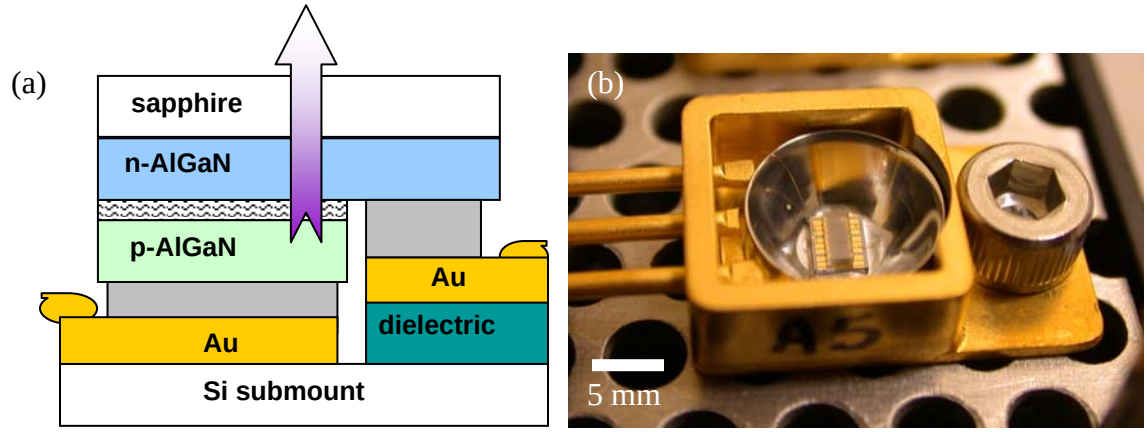

Figure 2. (a) Schematic of flip-chip-bonded deep UV LED on Si submount. (b) Photograph of a flip-chip LED array mounted in a TO-257 package.

Our UV LED development efforts focused on optimizing the performance of 250-280 nm LEDs. We succeeded in achieving three significant advances in device performance: (1) demonstration of higher power 270-280 nm LEDs, (2) demonstration of longer 270-280 nm LED operational lifetimes and (3) development and characterization of LEDs with wavelengths near 250 nm for possible application to nuclear materials sensing. Below we describe our device achievements in more detail.

Before the start of this LDRD, our Sandia team had demonstrated a maximum output power of 1.3 mW from 276 nm emitting 1mm x 1mm LEDs at 400 mA input current [3]. Operation beyond that current resulted in rapid and permanent device degradation. One expected limitation of those devices was the fact that they were grown on AlGaN-on-sapphire templates with relatively high (> $2x10^{10}$ cm^{-2}) dislocation densities. A major focus of our efforts was therefore to explore a wide range of growth conditions to optimize the AlN nucleation layer which largely defines the dislocation density of the overlying device epilayers. We succeeded in developing a distinct, patent-pending approach to producing AlN nucleation layers which resulted in total

dislocation densities in the overlying $A_xlGa_{1-x}N$ (x = 0.50-0.70) epilayers of 2-3x10^9 cm^{-2}. Growth of full LED heterostructures (similar to that shown in Figure 1) on these lower dislocation density templates resulted in a number of performance improvements. In Figure 3a, we show light output versus current and current-voltage data for a 1 mm x 1 mm LED on these lower defect templates with emission of ~277 nm. Beyond improved output power at 400 mA (1.78 mW vs. 1.3 mW), we achieved higher current operation before device failure. In particular, maximum output powers of 2.4 mW have been achieved at 600 mA DC operating conditions, representing a nearly 2X increase in achievable output power. In Figure 3b, we show the electroluminescence spectra as a function of operating current. The emission is strongly dominated by quantum well (QW) emission at 277 nm with below bandgap emission (~ 415 nm) due to defects having a peak intensity 500X lower than that of the QW emission. We note that earlier generations of Sandia devices had more dominant deep level emission (deep level peak emission only 40X lower than the QW peak emission). In work completed before this LDRD project, we had identified that optimization of the AlGaN electron block layer was critical in reducing the deep level contribution to LED emission and these LED structures employ the improved electron block designs [3].

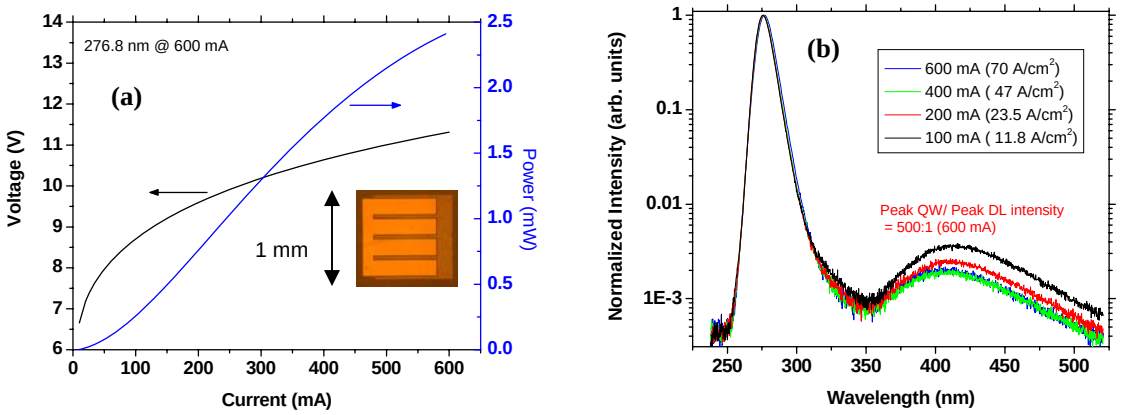

Figure 3. (a) Light output versus current and current-voltage data of new generation of 270-280 nm LEDs. Inset shows the interdigitated contact geometry for 1mm x 1mm LED. (b) Electroluminescence spectra for 1mm x 1mm LED at various operating currents.

We further optimized the performance of smaller area (300 μm x 300 μm) 270-280 nm LEDs and worked to demonstrate improved operational lifetimes. Our materials studies focused on two main areas for lifetime improvements: dislocation density reduction (described above) and improvement of surface morphology. Our focus on these areas was motivated by our observations that the signatures of LED degradation suggested a current leakage mechanism that may be related to defects. Further, evidence of spatially non-uniform light emission suggested that surface roughness may be causing non-uniform current injection, which was another possible failure mechanism. While growth on lower defect density AlGaN templates served to reduce defect densities in the LEDs, we further optimized the growth and design of the top layers of the device, namely the p-type AlGaN and GaN layers, to reduce surface roughness of the LEDs. In particular, atomic force microscopy (AFM) studies revealed a 3D-like growth morphology of p-GaN layers on the underlying p-AlGaN electron block layers of the device (Figure 4a) which likely resulted in non-uniform current injection. Optimization of the design

and growth conditions of these layers enabled a significantly smoother and more continuous surface (Figure 4b).

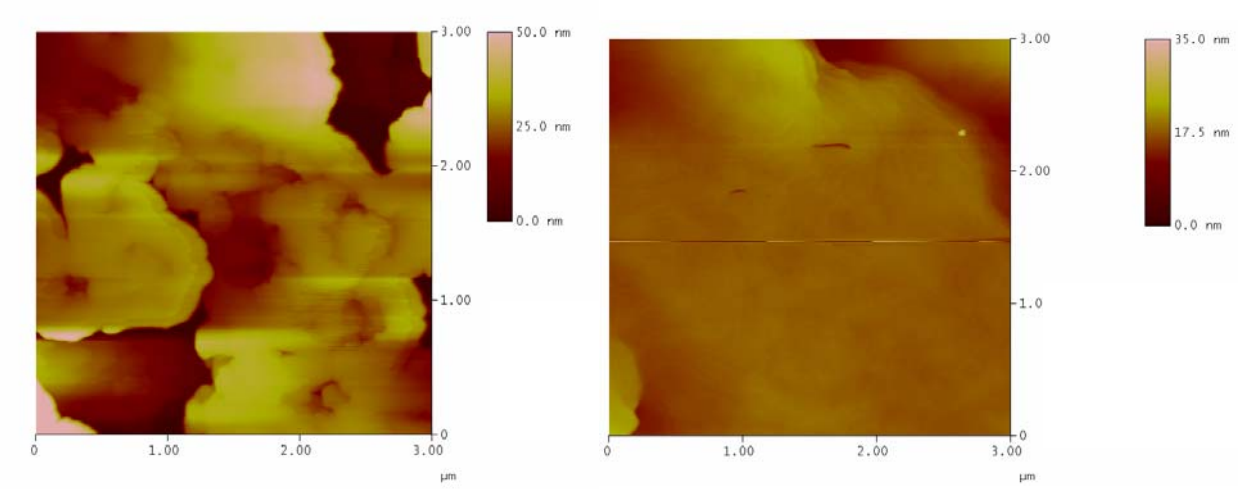

Figure 4. Atomic force microscopy images of (a) earlier generation LEDs with rough surface morphology and (b) latest generation devices with smoother surface morphology.

In Figure 5, we show lifetime data of a 271 nm emitting 300 μm x 300 μm LED with both reduced dislocation densities and improved surface morphology. The output power was monitored by a calibrated silicon photodiode while the device was operated at a constant current of 30 mA DC. We see that this device, which started at an output power of 90 μW, has only degraded 27% in almost 200 hours, with fairly stable voltage characteristics. This represents a notable advance in device lifetime (previous generation devices suffered > 50% power drop in

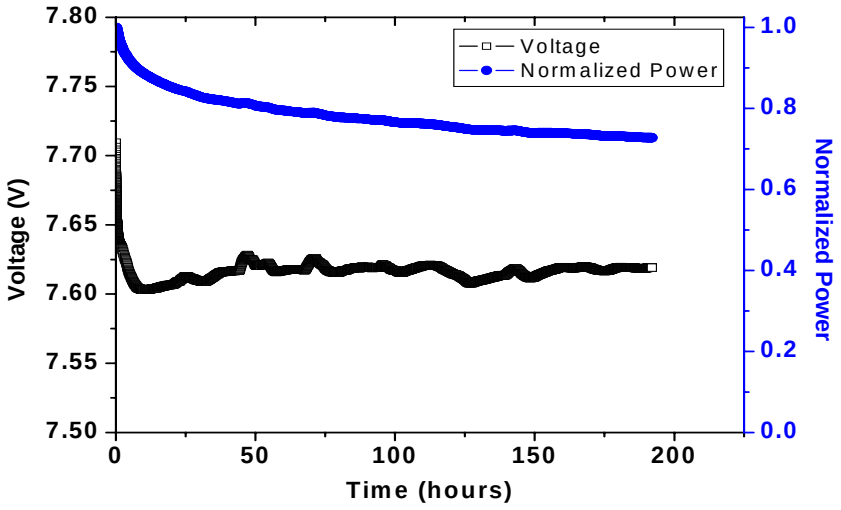

Figure 5. Lifetest data for a 300 μm x 300 μm LED emitting at 271 nm. Test was performed at 30 mA DC with the device starting power of 90 μW.

10-100 hours at these wavelengths), and demonstrates operational lifetimes sufficient for our biosensor system evaluations. Extended lifetime studies of these LED structures have demonstrated operational lifetimes (less than 50% power degradation) of > 1500 hours.

LEDs from this generation of device design were fabricated, flip-chip bonded onto Si submounts and packaged on TO-headers for delivery to the biosensor team. Typical output powers from individual 300 μm x 300 μm devices were ~0.16 mW at 30 mA, with highest output powers of ~0.18 mW at 30 mA. The output power for each device was measured using an integrating sphere and thus represents the total power available from each device at a given current---typically not all of the power could be effectively collected and delivered to the sample in our biosensor platforms. Given that our Sandia LED development efforts focused exclusively on the shorter wavelength 270-280 nm region, we augmented these home-developed devices with 340 nm LEDs from Sensor Electronic Technology, Inc. (a small US company that has recently commercialized deep UV AlGaN LEDs). Typical performance specs for SET devices purchased in early 2006 included output powers of ~0.30 mW at 30 mA and at peak wavelengths in the 337-339 nm range. These performance values were determined from our own measurements using our calibrated integrating sphere set-up.

We further pursued the development of AlGaN LEDs with emission at wavelengths shorter than 280 nm as these wavelengths could yield higher fluorescence yields from thin layers of nuclear materials. We note that atmospheric absorption of these short excitation wavelengths would render them non-ideal for long-range sensing, however, short range sensing approaches, including surface-scanning sensors, could reap the benefits of shorter excitation wavelengths. The demonstration of LEDs with emission in the 250-255 nm range required the development of $Al_xGa_{1-x}N$ n-type epilayers with $x \geq 0.70$. Our quantum well active region consisted of three $Al_{0.59}Ga_{0.41}N$ QWs with $Al_{0.72}Ga_{0.28}N$ barriers (compositions estimated from x-ray diffraction measurements of calibration samples and not actual device samples). Samples were fabricated into 300 μm x 300 μm LEDs with interdigitated contacts and flip chip bonded to Si submounts.

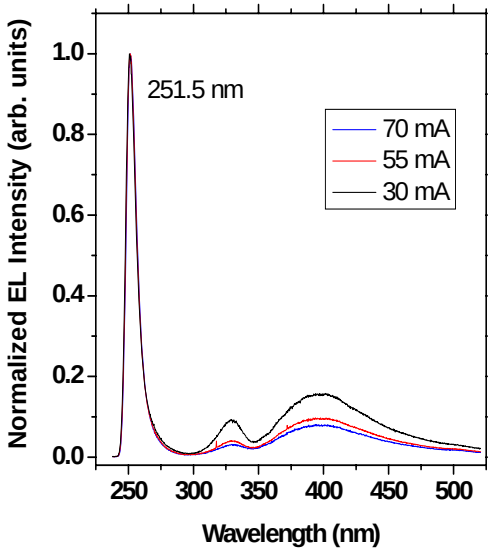

Figure 6. Electroluminescence spectra from 250-255 nm LEDs for various injection currents.

The devices were subsequently packaged into TO-257 headers with an integrated aluminum reflector cup. In Figure 6, we show electroluminescence (EL) spectra of an LED as a function of injection current. We see a primary peak from quantum well emission at 251.5 nm and the additional presence of below-bandgap emission from defect states in the 320 nm and 400 nm region. These defect peaks are more pronounced in these LEDs compared to our 280 nm devices (note the linear scale here), and is a signature of relatively higher defects in these higher bandgap alloys. We further characterized the output power from this LED and found low powers of approximately 10 μW at 30 mA. This performance is not atypical for immature LED technology at shorter wavelengths, but significantly improved output powers are needed before effective implementation into the biosensor platform.

These LED optimization efforts succeeded in achieving 270-280 nm LEDs with sufficient output powers and operational lifetimes for use in our biosensor development work. While further performance enhancements would clearly be beneficial, we instead focused our efforts on the more challenging task of developing deep UV AlGaN LDs. Below we describe those efforts.

2.3 Deep UV AlGaN Laser Diode Development Efforts

Our work toward AlGaN LDs resulted in significant advances in many critical areas but ultimately fell short of our aggressive final goal of achieving a pulsed 340 nm AlGaN LD by the end of the project. As described below, we made notable progress in the development of AlGaN QW active regions and demonstrated 339 nm optically pumped lasing from QW waveguide structures. We further demonstrated 10 ohm-cm resistivities in p-type AlGaN and applied those doping strategies to full separate confinement heterostructure lasers with minimal cracking and overall good structural integrity. On-wafer testing of those structures demonstrated dominant electroluminescence at 345 nm, and optimization of the design of those structures was performed. By the end of the program (September, 2007), we had also developed a range of required laser fabrication processes in Sandia's new MESA cleanroom facilities, but had not yet completed a full process run for ridge waveguide lasers. Nevertheless, our work in this project has brought us significantly closer to overcoming the challenges of a deep UV laser demonstration. In this section, we describe our accomplishments toward that goal.

Given the challenge of demonstrating p-type doping, our initial efforts to optimize AlGaN QW laser active regions focused on undoped structures and optical pumping (OP) experiments. Our UV LED development to date had employed sapphire substrates, however sapphire does not share a common cleavage plane with epitaxial AlGaN and therefore one must resort to more lossy plasma-etched laser mirror facets rather than the more conventional cleaved facets of most III-V lasers. In contrast, AlGaN structures on SiC substrates can be cleaved and have the added benefits of better thermal conductivity than sapphire. Our materials growth effort therefore involved substantial effort to develop a nucleation and growth process for AlGaN on SiC substrates. Following these development efforts, we grew AlGaN laser heterostructures on SiC substrates with a target wavelength of ~ 330-340 nm. The structures included six 3 nm thick $Al_{0.10}Ga_{0.90}N$ quantum wells with 7.0 nm $Al_{0.25}Ga_{0.75}N$ barriers. This active region is surrounded by 70 nm thick $Al_{0.25}Ga_{0.75}N$ waveguiding layers, as well as a bottom $Al_{0.35}Ga_{0.65}N$ cladding layer that is 250 nm thick. The entire structure is grown on 1.1 μm thick AlN on a 2" diameter SiC substrate.

We further completed process development efforts that have enabled relatively smooth laser mirror facets using a scribe and break process. The AlGaN OP laser structures on SiC substrates were lapped down from ~250 μm to 50-60 μm and application of our optimized cleaving process yielded facet RMS roughness values of ~1.2 nm. We constructed an optical pumping set-up based on a frequency quadrupled, Q-switched Nd:YAG laser with approximately 14 mJ pulse energy at 266 nm. Laser excitation regions of ~50 μm in width were defined on the AlGaN laser samples with a cylindrical lens and a 4f imaging system and typical cavity lengths for optical pumping experiments were in the 0.5-2 mm range. In Figure 7, we show an example of emission that was achieved from a 1 mm long cavity showing stimulated emission at 338.8 nm.

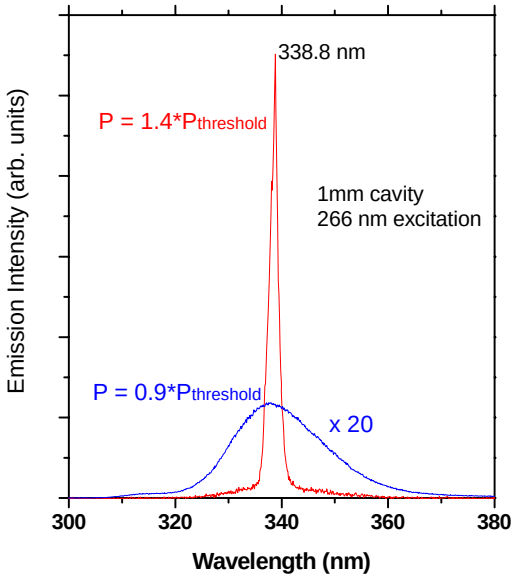

Figure 7. Emission spectra of optically pumped AlGaN laser structure at pump powers below (blue) and above (red) threshold.

In parallel with these optical pumping studies to optimize active region designs, we conducted intensive materials growth studies to achieve effective p-type doping in $Al_xGa_{1-x}N$ alloys in the x = 0.30-0.35 range needed for 340 nm laser structures. Key growth parameters that we examined include growth temperature, V-III ratio, and flow rate of the Mg dopant source material (Cp_2Mg). In addition, we carried out post-growth rapid thermal anneal studies to evaluate the temperature and time requirements to best activate Mg acceptors in our p-AlGaN samples. These combined efforts enabled the demonstration of p-type resistivities as low as 10 Ω-cm for $Al_{0.30}Ga_{0.70}N$ alloys using post-growth anneal conditions of 900ºC for 5 minutes in N_2.

These p-type doping studies showed sufficient progress that we moved forward with the development of full separate confinement heterostructure p-i-n diode laser structures. In Figure 8, we show a schematic of a typical target structure. Unlike the UV LEDs shown in Figure 1, these LDs structures include relatively thick AlGaN cladding layers as well as lower bandgap AlGaN waveguide layers around the QW active region to provide effective mode confinement.

In particular, these LD structures require much thicker p-AlGaN layers to properly confine the mode away from absorptive p-GaN contact layers. We initiated growth efforts on sapphire substrates which are significantly lower cost that SiC substrates and would allow for many growth iterations of our laser structures. Our growth efforts included a number of structures where we optimized the Mg-doping profiles and waveguide designs. The effectiveness of these design iterations was initially judged by on-wafer electroluminescence measurements, where we applied p-type and n-type contacts to allow LED-like structures but did not perform full laser waveguide fabrication. In Figure 9, we show an example electroluminescence spectrum from one of our full laser structures with 100 mA injected current. This spectrum reveals dominant emission at 345 nm upon electrical injection, showing the viability of our laser structures for providing emission near our 340 nm target wavelength.

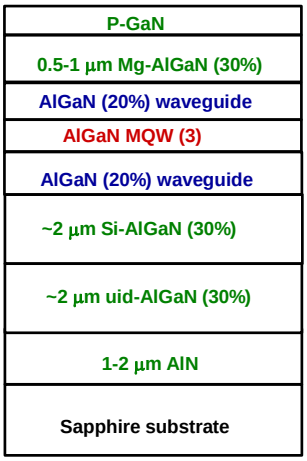

Figure 8. Schematic of p-i-n AlGaN laser diode structure. Percentages listed in schematic are Al compositions of AlGaN alloys for each layer.

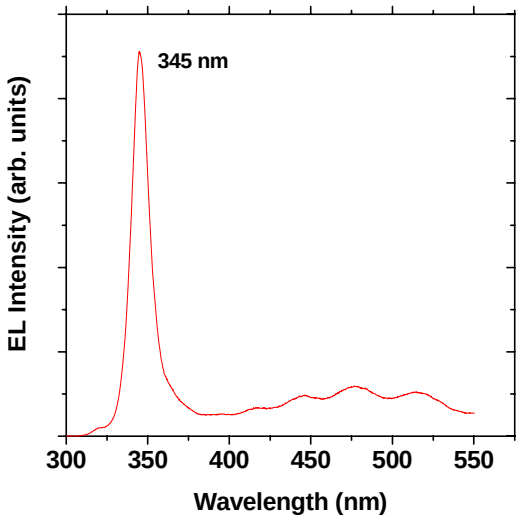

Figure 9. Electroluminescence spectrum from an AlGaN p-i-n laser diode structure (similar to that shown in Figure 8) under 100 mA injection current.

An additional requirement for our laser diode demonstration was the development of a laser diode fabrication process in our new MESA cleanroom facility. Throughout the last several months of this project, we focused our device development efforts on bringing up these required processes. As described earlier, our laser facet development focused on demonstrating smooth, cleaved facets from AlGaN laser structures on SiC substrates and we achieved ~1.2 nm RMS roughness from our optimized scribe and break process. This roughness is similar to that achieved for InGaN/GaN based visible laser diodes on SiC substrates [10]. In addition, we developed a process for e-beam evaporation of SiO_2/HfO_2 multi-layer stacks as high reflectivity facet coatings. In Figure 10, we show both model prediction and experimental data for the absolute percent reflectance from a 4 period multilayer stack. Target thicknesses were ~40 nm for the HfO_2 layers and ~57.8 nm for the SiO_2 layers for a stack to achieve a peak reflectance at our 340 nm target wavelength. We see that our experimental structure succeeded in demonstrating 90% reflectance at 340 nm.

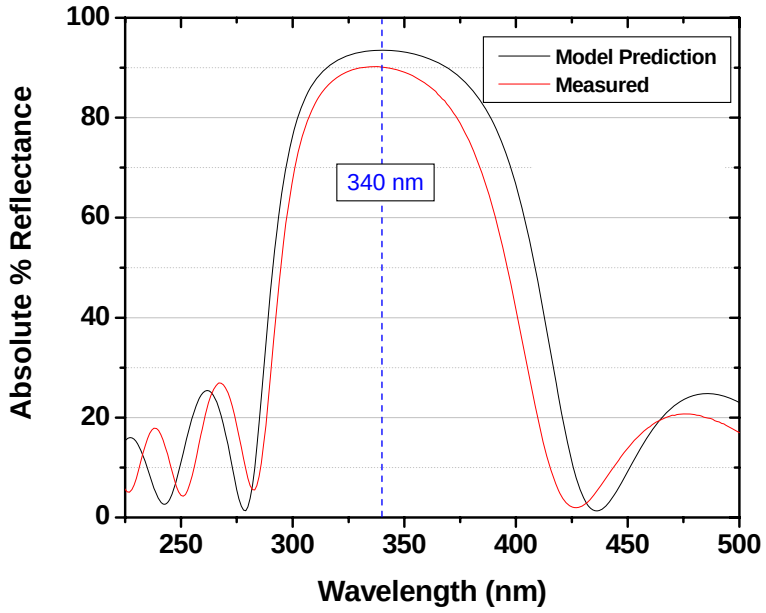

Figure 10. Absolute percent reflectance from a 4 period SiO_2/HfO_2 multilayer stack, showing both model predictions (black curve) and experimental data (red curve).

Further effort was applied to the optimization of Ti/Al/Mo/Au contacts that were originally developed for deep UV LEDs, as well as Pd/Au contacts to p-GaN. Inductively coupled plasma etching studies using BCl_3/Cl_2 were performed to optimize sidewall profiles while minimizing etch damage for both mesa and ridge waveguide definition. Finally, a new mask set was designed for both broad area and ridge waveguide laser diode fabrication.

3. Sensor Development

The second part of this LDRD project was devoted to exploring techniques to best use UV LEDs and semiconductor lasers in sensors to detect biological and nuclear materials. Although blue LEDs are already used in (inexpensive) biosensors, these sensors suffer from high false-alarm rate primarily due to the low power levels of the source (and subsequently low signal levels) and lack of spectral discrimination (simply measuring band-integrated fluorescence vs. wavelength-resolved fluorescence). The low signal light levels in these sensors are the result of using a low-power continuous wave (CW) device to illuminate a single bio particle while it traverses a small measurement volume. In addition, the fluorescence is usually detected using a single detector monitoring a wide spectral bandwidth. Thus, the sensor is not always able to discriminate between bio aerosols and some fluorescent background particles such as diesel smoke. Based on our experience with long-range standoff lidar systems for detecting biological aerosols, spectrally resolved fluorescence measurements greatly increase the probability of making a correct discrimination of bio vs. non-bio. In this work, we explored the feasibility of using LEDs in frequency-domain (i.e. modulation spectroscopy) techniques along with spectrally-resolved detection.

There are two basic approaches to fluorescence measurements for sensing biological or other materials: time-domain techniques and frequency-domain techniques. To date, time-domain measurements have been used almost exclusively for biosensors, although there has been some research conducted on frequency-domain techniques. Most time-domain techniques use a short-pulse laser to excite fluorescence from the biological material and use time-gated detection of the fluorescence as illustrated in Figure 11. By adjusting the time delay between the excitation pulse and the detection period, one can reduce the effect of background light and eliminate elastically scattered laser light, thereby greatly improving the fluorescence signal-to-background ratio and increasing the sensitivity of the instrument. In addition, for long-lived species, such as uranium-

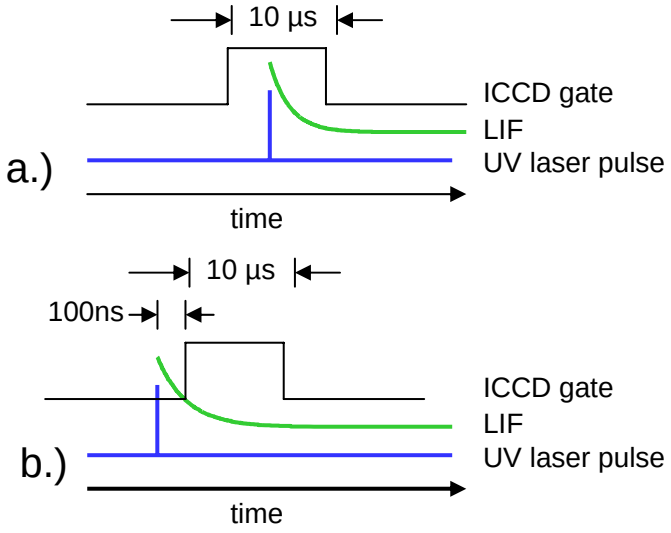

Figure 11. Example of time-domain laser-induced fluorescence techniques for a) prompt fluorescence; and b) delayed fluorescence which eliminates elastically scattered excitation light.

containing minerals (τ ~ several μs), for example, delayed fluorescence detection can greatly reduce the contribution of short-lived fluorescence from background materials. Although LEDs or laser diodes can be pulsed for use in time-domain measurements, they are at a distinct disadvantage in this mode of operation because of the low power available with an LED (or even a laser diode) compared to a Q-switched laser (even a microchip laser).

LEDs and laser diodes are much better suited for use with frequency-domain techniques (such as modulation spectroscopy), as illustrated in Figure 12. Here, the output power of the UV LED (or laser diode) is sinusoidally modulated at angular frequency $\omega = 2\pi f$. The resulting fluorescence is also modulated at frequency ω, but with a phase shift $\phi = \text{atan}(\omega\tau)$ that depends on the fluorescence lifetime of the material, τ. By using phase-sensitive detection techniques, one can reduce the undesirable background light, including elastically scattered excitation light, analogous to gated detection in time-domain techniques, and achieve relatively high fluorescence signal-to-background ratios. (An excellent overview of both time- and frequency-domain techniques for measuring the lifetime of fluorescent materials is given in Reference 11.)

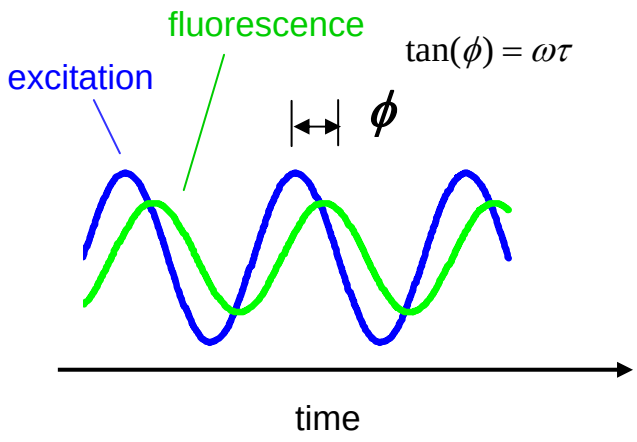

Figure 12. Example of a frequency-domain (or modulation spectroscopy) fluorescence technique.

In this LDRD, we conducted experiments using several different frequency-domain test-bed configurations, including single-channel (band-integrated fluorescence) photomultiplier tube (PMT) and multi-channel (spectrally resolved) PMT detection. The following sections describe these experiments, their results, and some of the conclusions we have drawn from these experiments regarding the potential of LED-based fluorescence instrumentation.

As shown in Figure 12, when the intensity of the excitation light is modulated, the resulting fluorescence signal is also modulated at the same frequency and experiences a phase shift ϕ. In addition, the depth of modulation of the fluorescence signal, m, depends on the frequency and the fluorescence lifetime: $m = (1 + \omega^2\tau^2)^{-1/2}$ (see Ref. 11). The relationship between phase shift and modulation depth as a function of modulation frequency is plotted in Figure 13. We can see from this plot that there is range of modulation frequencies that yield a good compromise

between adequate phase shift (for discrimination using phase-sensitive techniques) and adequate modulation depth (which will determine the magnitude of the fluorescence signal detected). For a fluorophore with a single exponential decay lifetime and a sensor using a single modulation frequency, the optimum modulation frequency is $\omega \approx 1/\tau$ or $f = 1/2\pi\tau$. For biological detection, for example, the NADH-related signature has a fluorescence lifetime of $\tau \approx 3$ ns, resulting in an optimal modulation frequency of $f \sim 100$ MHz. As we show later in this report, this is well within the modulation readily achievable with LEDs and semiconductor laser diodes. As another example, many uranium-containing minerals have fluorescence lifetimes $\tau \sim 3$ µs (or longer, depending on their local environment), which requires a modulation frequency of $f \sim 100$ kHz. This lower modulation frequency is certainly within the capabilities of LEDs and laser diodes, and, in fact, allows the use of much simpler and less expensive diode drivers and phase-sensitive detection circuits than the higher-frequency bio detector.

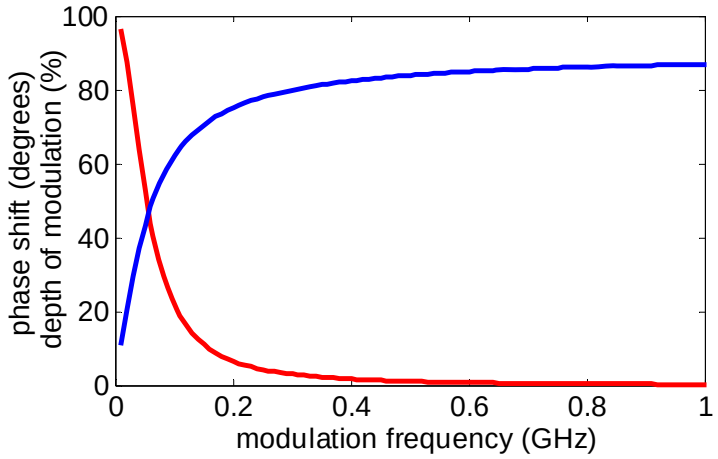

Figure 13. Simulated phase shift and depth of modulation versus modulation frequency for a fluorophore with fluorescence lifetime $\tau = 3$ ns (typical of the NADH-related bio signature). Here, the optimum modulation frequency is $f \sim 100$ MHz. For a fluorophore with fluorescence lifetime $\tau = 3$ µs (typical of uranium-containing minerals), the optimum modulation frequency is $f \sim 100$ kHz.

3.1 Electrical Measurements of Deep UV LEDs

The electrical characteristics of the LEDs as a function of frequency are important because they determine both the drive circuit requirements and the maximum useful modulation frequency that we can operate a given LED. We measured the complex RF reflection coefficient (S_{11}) of 340- and 280-nm UV LEDs using an HP 3577B Vector Network Analyzer (VNA) over a frequency range of 0.1 to 200 MHz, thereby allowing us to determine the RF impedance of the LEDs. A typical S_{11} measurement is shown in Figure 14 (a), along with the best fit to the data assuming the equivalent RF circuit model of the UV LED shown in Figure 14 (b).

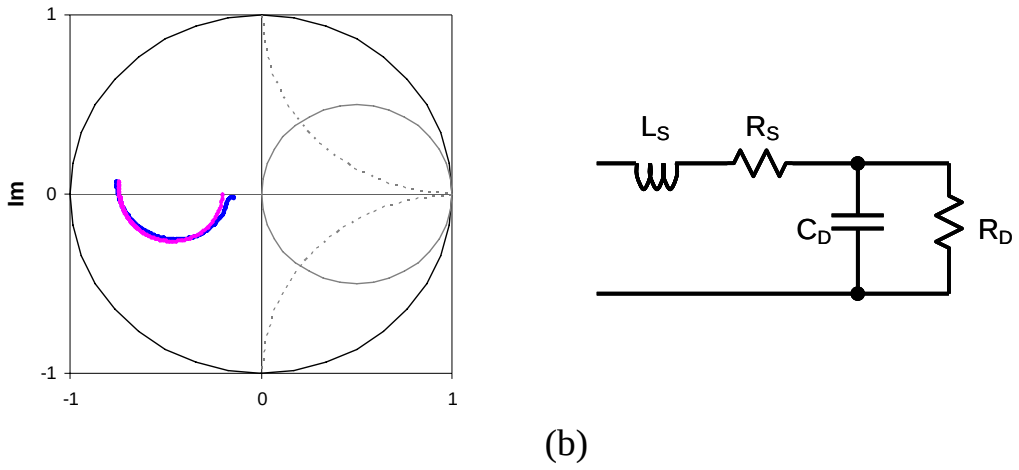

Figure 14. (a) Network analyzer S_{11} measurements (blue trace) of 340-nm LED (DC biased at 14 mA) from 0.1 to 200 MHz and fit (pink trace) to data. (b) RF equivalent circuit of LED used to extract impedance values from measured S_{11} data.

Table 1 summarizes the fit parameters to S_{11} measurement data from 340- and 280-nm LEDs at various DC bias currents. Note that, as expected, the differential resistance of the diode decreases as the bias current increases, and the other circuit elements are essentially constant versus bias current. The observed variations in fit parameters versus bias current suggest that we could have chosen a more accurate (but more complicated) equivalent circuit model than the one shown in Figure 14b.

Table 1. Impedance model fit parameters for 340 and 280-nm LEDs at various DC bias currents.

File	Device	I(mA)	R_D(Ohm)	C_D(pF)	R_S(Ohm)	L_S(nH)
060420E	UVT340	5	55.6	291	6.86	4.00
060420C	UVT340	8	35.5	302	6.97	3.83
060420D	UVT340	14	26.2	315	6.95	3.78
060420F	UVT280	5	52.5	254	12.38	0.21
060420G	UVT280	14	30.5	260	11.59	0.48

We also measured the frequency response (S_{21}) of a 340-nm LED, from the LED input to the photodetector output, as shown schematically in Figure 15 (a). The photodetector was either a photomultiplier tube or a New Focus amplified photodiode. The frequency response data measured from a 340-nm LED biased at 14 mA are shown in Figure 15 (b), which indicates a bandwidth slightly less than 100 MHz. As discussed previously, 100 MHz is the required frequency to optimally discriminate bio materials which have fluorescence lifetimes $\tau \sim 3$ ns. The ripple on the frequency response data is likely due to electrical reflections between the UV LED and the network analyzer port, which differs slightly from the ideal 50 ohms. Electrical phase shift versus frequency information was simultaneously obtained during our measurements but is not shown in the plots below. Interestingly, the photomultiplier tube showed significantly

higher gain than the amplified photodiode, but it also exhibited approximately 3*360 degrees of phase shift at 200 MHz that was not observed from the photodiode detector.

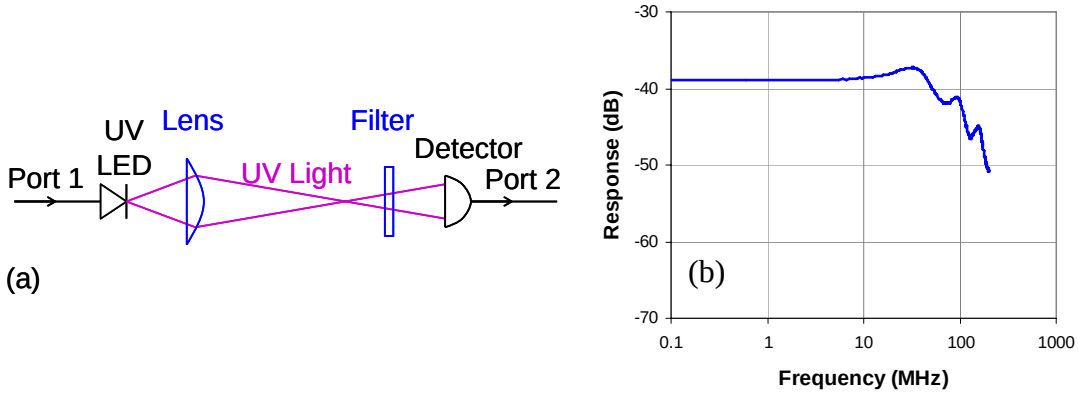

Figure 15. (a) Schematic of S_{21} frequency response measurements. (b) Frequency response S_{21} (amplitude) data from 340-nm LED (DC biased at 14 mA) from 0.1 to 200 MHz using a photomultiplier tube detector.

3.2 Fluorescence Experiments with Deep UV LEDs

The next sections of this report describe a number of experiments using the UV LEDs with various modulation spectroscopy techniques. We built a single-channel (i.e. band-integrated) fluorimeter and used it to measure the lifetime of a number of standard fluorescent species with lifetimes comparable to the bio species. These measurements basically confirmed that our modulation spectroscopy setup was working properly: that is, we were able to drive the LEDs at frequencies up to 100 MHz, and that we were able to use phase-sensitive detection to acquire the fluorescence signal and process the data to obtain the proper lifetime. Next we built a multi-channel fluorimeter testbed using a compact spectrometer to disperse the fluorescence spectrum and a multi-anode PMT to detect it. We used the spectrally-resolved fluorimeter to measure spectra of both bio materials (ns decay times) and uranyl nitrate (μs decay times) and measured the detection sensitivity of the system for uranyl nitrate and compared it to the sensitivity of two other methods.

Single-channel (band-integrated) fluorimeter

Figure 16 shows the fluorimeter that we built, using Sandia-fabricated 280-nm LEDs, to measure the fluorescence lifetime of a laser dye and several biomaterials. The outputs of an RF signal generator and a low-noise DC current source are combined in a bias tee to drive the LED. UV emission from the LED passes through a 25-nm-wide bandpass filter centered at 280 nm and illuminates a quartz cuvette containing solid or liquid bio samples. Fluorescent light is isolated from elastically scattered light by a dielectric long-pass filter (Barr 320 nm LP) and detected by a large area PMT (Hamamatsu R2368). Because much of the light produced by the LED can not be easily collected by a lens and focused to a small spot, we found direct illumination of the sample actually increased fluorescence detected from the sample. Although lenses could have been used to collect the fluorescence, the detection area of the PMT is large enough that we are

able to detect a significant amount of fluorescence without them. The amplitude and phase of the modulated fluorescence signal is measured by a commercial high-frequency lock-in detection system (Stanford Research model SR844).

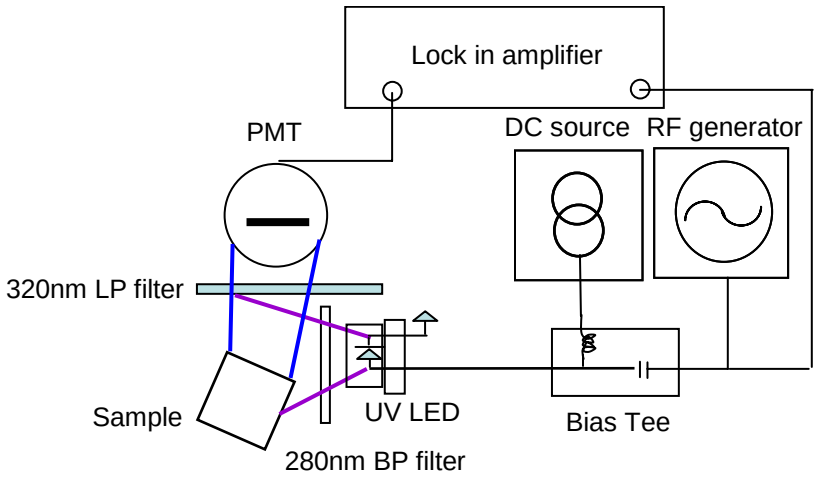

Figure 16. Schematic diagram of frequency domain fluorimeter. The LED is biased with d.c. current and an a.c. modulation is added using a bias tee. An RF splitter before the bias tee (not shown) sends half of the RF signal reference the lock in. The red emission tail of the LED illumination is removed by a 25-nm-wide band pass filter centered at 280 nm. Elastically scattered LED light is separated from the fluorescence using a dielectric 320-nm long pass filter. The phase of the fluorescence modulation with respect to the signal generator is measured using a lock-in amplifier. The measurement is repeated with a scattering target without the long pass filter to measure the scattering phase. The fluorescence phase shift at a given modulation frequency is the difference of these two measurements.

We used this fluorimeter to measure the fluorescence lifetimes of four samples including three bio-molecules: Coumarin 440 (a laser dye) in MeOH (1.4 mM), L-tryptophan (dry), N-acetyltryptophanamide or NATA (9 mM in 0.01 mM Tris pH 8.0), and Trypticase soy broth (dry). When the phase of the fluorescence signal (with respect to the lock in reference) is subtracted from the phase scattered light from a non-fluorescing target ($BaSO_4$), the fluorescence lifetime can be calculated from the phase shift. Assuming a single exponential decay, the lifetime, τ, is related to the phase shift, ϕ, by $\phi = \text{atan}(\omega\tau)$, where ω is the modulation frequency. This expression can be generalized to include multiple exponential decays or other functional forms for fluorescence decay. Plots of ϕ vs. ω are shown in Figure 17 and lifetimes have been calculated from a fit of each curve to $\tau = \dfrac{\tan(\phi)}{\omega}$.

We recovered lifetimes of 2.8, 4.4, 3.4 and 4.2ns ± 0.3 ns for NATA, Coumarin 440, Tryptophan and Trypticase soy broth, respectively. Measurements on NATA and Coumarin 440 are in agreement with published values for these systems. During these investigations, we found the elastically scattered light from dry bio-samples (Tryptophan, Trypticase soy broth) under typical amounts of illumination saturated our detector when the long-pass filter was removed. This demonstrates that using phase-sensitive detection alone is not adequate for eliminating the elastically scattered background from highly scattering materials. Any practical fluorimeter will need to employ a long-pass filter to eliminate elastically scattered light. As a side note, the same

is true for time-domain instruments using gated detection: the on/off ratio for an intensified CCD is not high enough to completely eliminate the elastically scattered signal, and these systems, too, require the use of long pass filter.

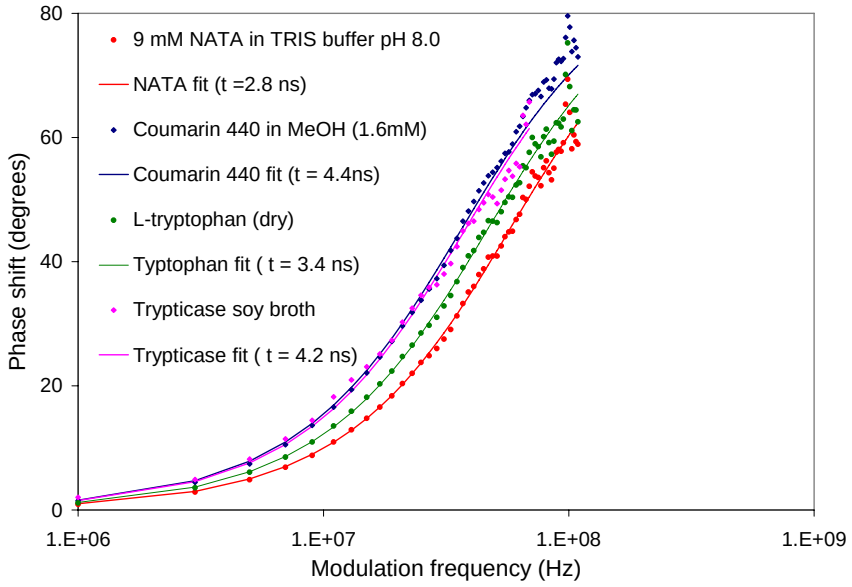

Figure 17. Plot of fluorescence vs. modulation frequency of NATA, Coumarin 440, L-Tryptophan, and trypticase soy broth. Fits of the data to equation X were used to calculate a lifetime for each sample.

In addition to lifetime measurements made on the single-channel fluorimeter, we measured wavelength-resolved spectra for each of the aforementioned samples on a time-domain system shown schematically in Figure . Light from a 274-nm UV LED passes through a 25-nm-wide band-pass filter centered at 280 nm (not shown) and illuminates the sample, which is contained in a standard 1-cm quartz cuvette. Fluorescent emission from the sample is collected by a set of UV achromats and imaged onto the entrance slit of imaging spectrograph (JY-CP140). As in the single-channel fluorimeter, a long-pass filter blocks scattered UV LED light from entering the spectrograph but allows the longer-wavelength fluorescence to pass. An intensified CCD (Princeton Instruments IMAX ICCD) system records the fluorescence emission spectrum from ~300 nm to >700 nm with a spectral resolution of ~10 nm FWHM (with the 0.5-mm-wide entrance slit used). The measured spectra for these materials are shown in Figure .

The peak fluorescence of Coumarin 440 and NATA are observed at previously reported wavelengths of 430 and 360 nm respectively. Dry tryptophan and trypicase soy broth have maxima near 330 nm (typical tryptophan signature in bio organisms), although the shape of the short wavelength band edges are obscured by the 320-nm turn-on of the long-pass filter. Typticase soy broth also contains signature at 440 nm typical of NADH.

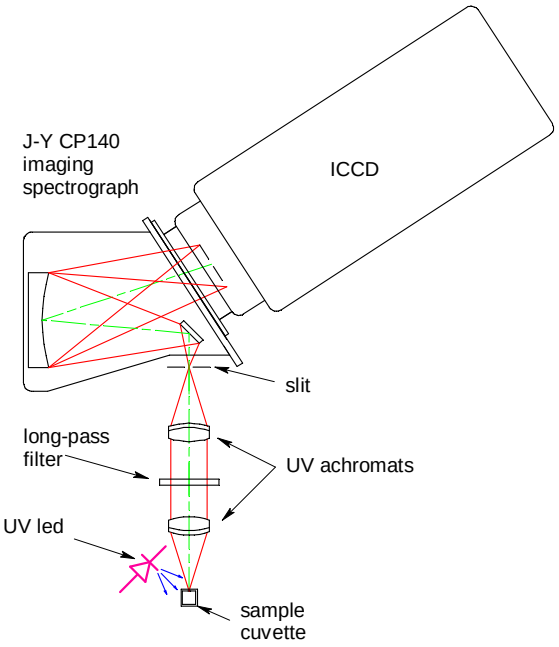

Figure 18. Schematic diagram of spectrally resolved UV fluorescence data collection system.

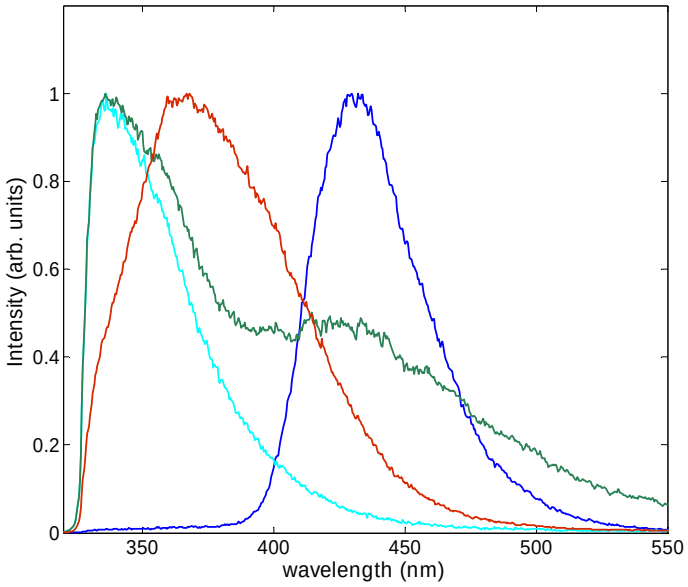

Figure 19. Normalized fluorescence spectra of Coumarin 440 in MeOH (blue), dry L-tryptophan (light blue), dry Trypticase soy broth (green), and 9 mM NATA in TRIS buffer (red).

Phase-sensitive spectrally-resolved measurements

One of the goals of this portion of the LDRD project was to build a testbed that combined modulated LED excitation with phase-sensitive and spectrally-resolved detection. The basic setup for this testbed is shown in Figure 20. A ball lens is used to image light from the UV LED

to illuminate the sample which is held inside a 1-cm quartz cuvette. Scattered and fluorescent light is collected by a pair of UV achromats and imaged onto the entrance slit of a compact imaging spectrometer (JY CP-140). A long-pass filter is used to reject the elastically scattered LED light. The spectrum is imaged onto a 32-channel multi-anode PMT (Hamamatsu H7260-04) which allows both time-resolved and spectrally resolved fluorescence measurements. The pixel spacing on the multi-anode PMT (MAP) is 1 mm and the dispersion of the spectrometer is approximately 17 nm/mm, resulting in ~20 nm spectral resolution for the device. Some representative spectra of biomolecules obtained using the spectrally dispersed frequency-domain system are shown in Figure 21.

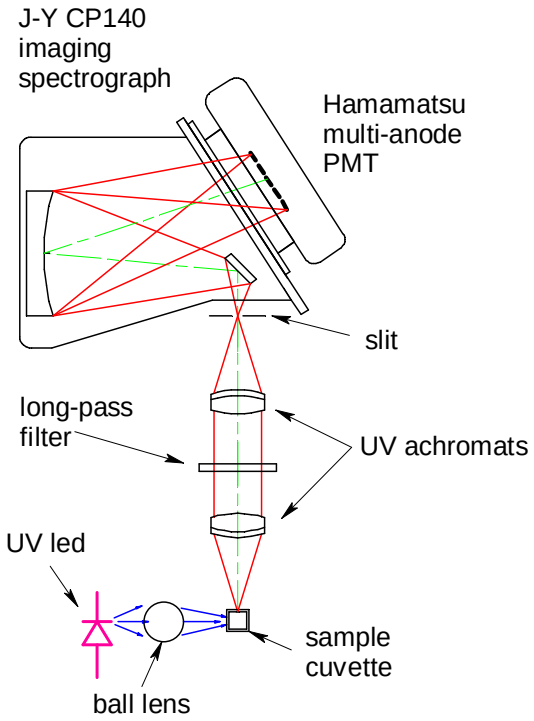

Figure 8. Experimental setup using UV LED excitation and spectrally dispersed detection using the J-Y CP140 imaging spectrograph and Hamamatsu multi-anode PMT.

Although the use of a dispersive spectrometer combined with the multi-anode PMT (MAP) can potentially produce very valuable data (using both spectral shape and lifetime information), it is a challenge to use a MAP detector in either a time-domain or a frequency-domain application because of the large number of channels to be digitized and processed. The current detector, with about 12 channels covering the useful part of the emission spectrum, will ultimately require a 12-channel lock-in detection system for use in an application. To perform our initial proof-of-concept experiments, we used a single high-frequency lock-in amplifier (the same Stanford research SR 844 is used previously) and measured each spectral channel serially. Ultimately, if modulation spectroscopy techniques are to be used in a real-time application, a miniature multi-channel lock-in amplifier needs to be developed or, if the time required for the measurement is not critical, then an RF signal multiplexer can be used to timeshare the phase-sensitive detector.

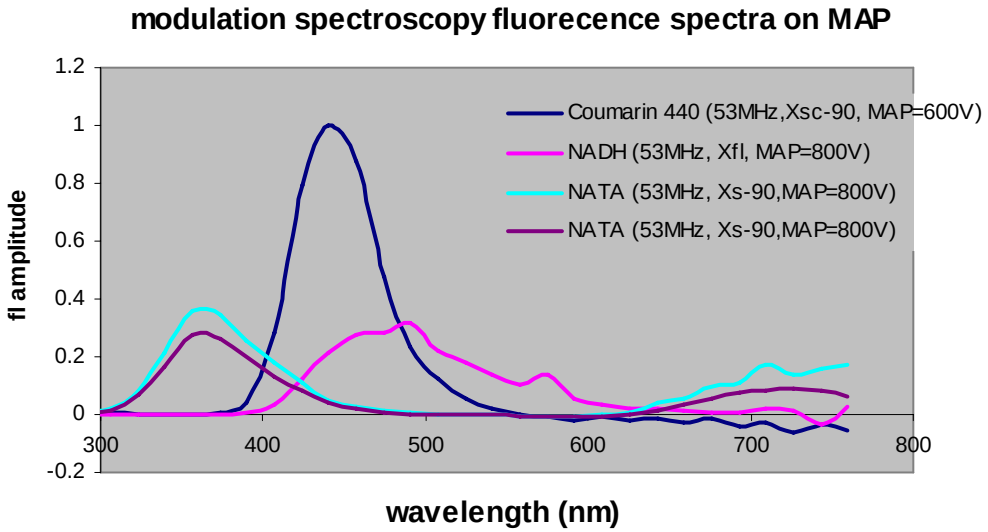

Figure 21. Representative spectra taken on the CP 140 with MAP detector and phase sensitive detection.

One of the most important advantages of using modulation techniques and phase-sensitive detection is that the elastically scattered light can be nearly eliminated from the signal (see ref. 12 for example). For weakly fluorescing species (or low concentrations), the magnitude of the elastically scattered light can be much larger than the fluorescent light, even when a long-pass filter is used to block elastically scattered light. Using phase-sensitive detection, we can take advantage of the fact that the fluorescence is phase shifted from the elastically scattered light. One particularly effective method is illustrated in a vector diagram of the signals in Figure 12. If the reference phase of the lock-in detector is chosen to align the signal from the elastically scattered light along the y-axis, then the signals detected 90° from this (i.e. along x-axis in the diagram) will, in principle, be free of any elastically scattered signal component. Although one could adjust the modulation frequency so that the phase shift between the fluorescence in the elastically scattered light is exactly 90°, in practice, this is difficult to achieve due to the high frequencies required, and, more importantly, the small depth of modulation of the fluorescence signal at 90° phase shift (see Figure 13). In these experiments, we operated modulation

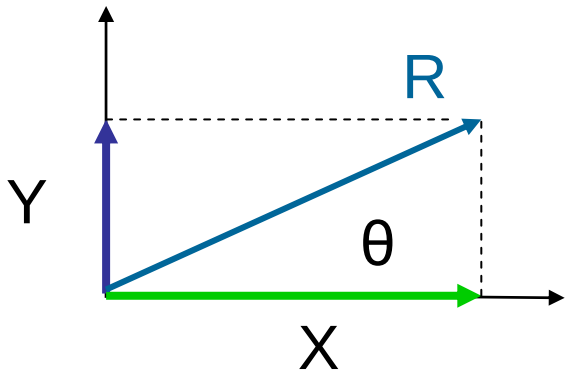

Figure 22. Vector diagram of the signals measured by lock-in detection. If the reference phase of the lock-in amplifier is chosen to place the purely elastic scattering light along the Y axis of the diagram, then the X component of the measured signal, R, contains no contribution from elastically scattered light.

frequencies that produce phase shifts near 45° for the fluorescence and accept the cos(45°) reduction of the fluorescence signal in exchange for near complete extinction of the elastically scattered light.

In order to demonstrate the effectiveness of using modulated LED illumination and phase-sensitive detection to discriminate against elastically scattered light, and to determine the potential sensitivity of these systems for analytes of interest to Sandia, we conducted a series of experiments to compare sensitivity and noise performance of three different systems: 1) a system with continuous UV LED illumination (so-called DC detection), 2) a system with modulated LED excitation and phase-sensitive detection, and 3) a microlaser-based time-domain system. The first two systems used the apparatus described previously and illustrated in Figure 20. The third system used a 355-nm microlaser for excitation (~2 ns pulse width), and an ICCD for gated detection, but was otherwise identical to the other two setups. All three setups used the same collection optics and CP-140 imaging spectrometer. For this set of experiments, we analyzed only one channel of the MAP detector, the channel containing the peak fluorescence. For the ICCD system, we analyzed the equivalent spectral bandwidth.

The analyte that we chose to use for this comparison is uranyl nitrate, $UO_2(NO)_2$, because one of the potential applications for an LED-based fluorescence sensor is detection of uranium. The uranyl ion (UO_2^{2+}) is a fluorescent ion that forms stable complexes with many soils and minerals in the environment (see refs 13 and 14). Although the fluorescence-based instrument would be expected to detect solid forms of uranyl-containing compounds, for this study we used liquid solutions of uranyl nitrate so that the concentration could be varied in a well calibrated way. Kathleen Holt (org 6772) prepared solutions of uranyl nitrate in 0.1 M nitric acid with concentrations of $2x10^{-4}$, $5x10^{-4}$, $1x10^{-3}$, and $2x10^{-3}$, and $1x10^{-2}$ M. These solutions were placed inside sealed 1-cm quartz cuvettes so they could be measured using the fluorimeters described above. In addition, one cuvette was filled with 0.1 M nitric acid solution to serve as a reference.

The results for the system with continuous 340-nm LED excitation and CW detection are shown in Figure 23. While this system did show some sensitivity to the variation in uranyl nitrate concentration, the noise (defined here simply as the standard deviation of repeated measurements) for each measurement was much greater than the average measured value itself. Note that the error bars in the plot indicate the standard deviation of each measurement. We observed that the noise characteristics of the multi-anode PMT are not favorable for the continuous high-signal levels. The detector operated much better in low signal level conditions – conditions amenable to photon counting or to the phase sensitive detection described below. In the case of CW illumination and detection, the MAP detector's dark current level and its associated noise was comparable to the signal levels from fluorescence. To obtain the data shown in Figure 23, we implemented a crude form of photon counting in an attempt to reduce the deleterious effects of the high dark current baseline. Based on the measured slope of the signal vs. concentration curve and the measured noise, we estimate the minimum detectable concentration for this system (assuming a signal-to-noise ratio of 3) is $3.1x10^{-2}$ M. This is not a useful detection limit for uranyl nitrate.

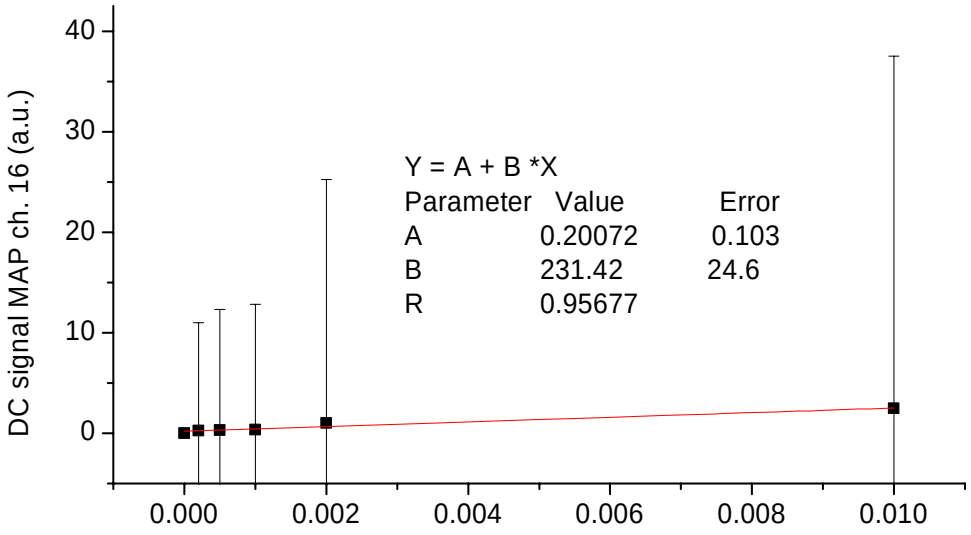

Figure 10. Plot of signal vs. concentration for uranyl nitrate solution using continuous UV LED excitation. In spite of the fact that a long-pass filter was used to block the elastically scattered light, there is still a huge uncertainty for each measurement due to the residual elastically scattered light.

The results of the sensitivity study for the modulated 340-nm LED and phase-sensitive detection system are shown in Figure . For this system, we modulated the LED at 90 kHz, resulting in about 60° phase shift of the fluorescence relative to the elastically scattered light. (The fluorescence lifetime of uranyl nitrate in solution in 0.1M nitric acid is about 3 µs, resulting in relatively modest modulation frequency requirements.) For these experiments, we adjusted the reference phase shift on the lock-in amplifier to place the elastically scattered light 90° from the detected fluorescence as described previously. In this case, the noise associated with each measurement is reasonably small (compared to the dc detection technique). The phase-sensitive detection eliminated nearly all of the elastically scattered light component. In addition, the phase-sensitive technique is able to eliminate most of the effects of the MAP detector's dark current and dark noise because these are not time-correlated with the LED modulation. For this system, we computed the minimum detectable concentration (SNR = 3 in a 0.5-second measurement interval and 20-nm spectral interval) equal to 3.7×10^{-5} M. If all spectral channels were used in a measurement (~10 channels), the minimum detectable concentration would further improve and it is possible that this technique may be sensitive enough for some uranium-detection problems.

Finally, we performed measurements on the uranyl nitrate samples using a microlaser-based time-domain instrument. It used short (~2 ns) 355-nm pulses produced by a microlaser to illuminate the sample and an intensified CCD to detect the spectrum (see ref 15 for more technical details on the time-domain system). The delay between the excitation pulse and the gated detection was 900 ns. This delay was long enough to exclude short-lived fluorescence from the quartz cuvette in addition to the elastically scattered light. Because the ICCD has higher spatial (and therefore spectral) resolution than the MAP detector, we de-resolved the ICCD data to have equivalent spectral resolution as the MAP detector systems before making the signal-to-noise and sensitivity calculations. Unfortunately, in this set of measurements, the blank

cuvette (with only 0.1M nitric acid) was not measured, and as a result, we do not have a direct measurement of the zero-concentration to determine background signal levels. However, based on detector-limited dark noise, the calculated sensitivity of the time domain system is about 1 x 10^{-6} M for a 1-second measurement and 20-nm spectral bandwidth. Results of this experiment are shown in Figure 25.

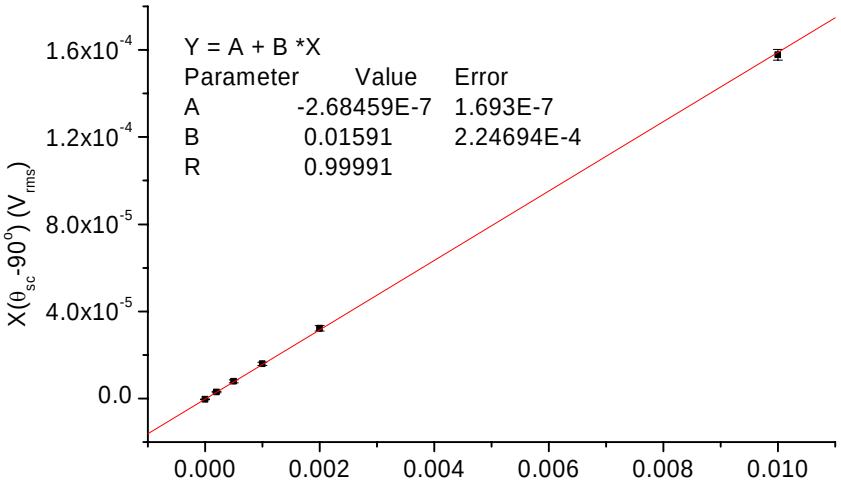

Figure 24. Plot of fluorescence signal vs. concentration for uranyl nitrate solution using 340-nm UV LED modulated at 90 kHz. Here the uncertainty in each measurement is very small due to the fact that the phase-sensitive measurement has blocked nearly all of the elastically scattered light.

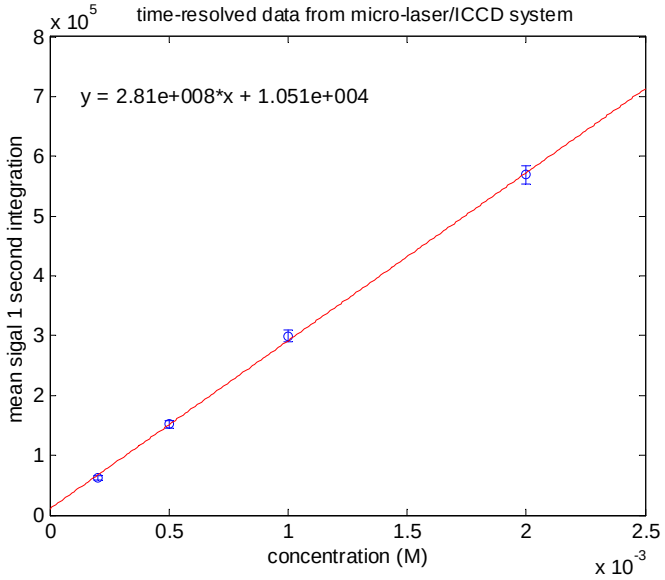

Figure 25. Plot of fluorescence amplitude vs. concentration for uranyl nitrate obtained using a time-domain system. The measurements were made 900 ns after the laser excitation pulse, thereby eliminating elastically scattered light and any short-lived (background) fluorescent light.

The results from the comparison are listed in Table 2. Here the modulated excitation and phase-sensitive detection technique is at least three orders of magnitude more sensitive than the continuous illumination and detection method. For this set of tests, the microlaser-driven time-domain technique was approximately an order-of-magnitude more sensitive than the LED driven frequency domain system. The total number of UV photons used to make the measurement in each case were comparable. One of the likely reasons for the better performance of the time-domain system is the extremely low dark noise of the ICCD compared to the relatively high dark-noise of the multi-anode PMT.

Table 2 Comparison of three different excitation/detection techniques

Detection method	Detection limit (SNR = 3; 20-nm bandwidth)
Continuous excitation – simple detection MAP detector single channel 340nm LED	3.1×10^{-2} M (dark noise limited)
Phase-sensitive measurement MAP detector; single channel 340 nm excitation; 0.5-sec data ave.	3.7×10^{-5} M
Gated time-domain detection 355-nm micro-laser / ICCD detector; 1-second data ave.	1×10^{-6} M (dark noise limited)

In addition to the uranyl nitrate solutions, we also measured surrogate bio materials NADH and NATA with the single-spectral-channel frequency-domain fluorimeter (Figure 16). These measurements (not presented in detail here) showed that for the short-lived bio fluorophores ($\tau \sim$ 3 ns) the UV LEDs could be modulated at the required frequencies (20 – 100 MHz) in order to obtain useful fluorescence phase shifts of 20º to 60°. Further, the phase-sensitive detection technique (using band-integrated fluorescence) was able to achieve detection limits for NADH in solution of $\sim 1 \times 10^{-8}$ M. Unfortunately, we cannot make a direct assessment of the detection limits for bio aerosol particles from these measurements since the fluorescence efficiency for the neat solutions used are much greater than the fluorescence efficiency from cultured organisms. Nevertheless, the results of these measurements indicate that LED-based frequency-domain fluorescence systems may have applicability for some sensor applications. As an example, the technique may be applicable for very-short-range (possibly ~6") standoff detection of bio particles on surfaces such as tables, floors, or walls. Here, the UV LED would broadly illuminate a small area on the surface (say several square inches) and a lens would collect fluorescent light and focus it onto a PMT. Both phase-sensitive detection and some form of multi-spectral detection would be necessary since many common man-made materials fluoresce with short lifetimes. Similarly, a sensor like this could be used to detect uranium on surfaces using the same hardware (albeit different modulation frequency).

4. Summary and Future Work

In this LDRD project, our team pursued the development of novel, compact, ultraviolet-emitting solid-state sources for fluorescence-based sensing applications. In concert with those efforts, we developed various fluorescence-based sensor testbed systems to evaluate sensing strategies to best take advantage of these new solid-state sources. Our goal was to evaluate the potential for these emerging UV light sources to enable a new level of compactness and flexibility while achieving high detection sensitivity and good discrimination against background signatures.

In the UV sources development portion of the LDRD project, we focused on improving the performance of 270-280 nm AlGaN-based deep UV LEDs for use in our biosensor development efforts. Our successful demonstration of AlN nucleation layers with reduced defect densities as well as improved LED surface morphologies led to notable increases in output power and device operational lifetimes. This effort succeeded in developing 270-280 nm LEDs with sufficient performance for evaluation of these devices in a number of biosensor platforms. We further explored the development of AlGaN-based 250 nm region LEDs, which may enable improved detection sensitivity for nuclear materials. These efforts were successful in demonstrating ~251 nm electroluminescence, however output powers were in the ~10 μW level and further performance advances are needed for application to our sensor systems.

Beyond advancing the performance of deep UV LEDs, our team pursued a very aggressive UV source milestone: the demonstration of the first UV laser diode at 340 nm. AlGaN-based deep UV LDs would enable greater performance in a sensor system than LEDs due to improved efficiency of light delivery, greater spectral purity, greater modulation speeds and possibly greater output powers, however they also present significantly greater challenges to their development. While our team did not demonstrate a fully fabricated laser diode structure by the end of the project, very significant progress was made toward that goal, including the development of AlGaN laser structures that demonstrated 339 nm lasing through optical pumping as well as the demonstration of full p-i-n separate confinement heterostructure laser samples with electroluminescence at 345 nm.

Overall, our project has shown the clear potential of AlGaN-based UV emitters to provide a new and compact source of deep UV excitation in fluorescence-based sensing systems, however further performance advances are needed to fully realize that potential. Future work must focus on materials advances, with a particular emphasis on reducing defects and improving p-type doping in these promising UV materials. In particular, we note that the difficulty of demonstrating effective p-type doping should only increase with higher bandgap, and thus for shorter wavelength sources (e.g. < 280 nm) alternative doping strategies and structures (e.g. short period Mg-doped superlattice structures) will likely be required.

In the sensor development portion of the LDRD project, we explored the efficacy of using modulated LED excitation and phase-sensitive detection techniques for fluorescence detection of bio molecules and uranyl-containing compounds – two areas of interest to Sandia. We built several testbed fluorimeters, including a spectrally dispersed unit that used a multi-anode PMT to provide multi-spectral detection. Although we were not able to advance the testbed hardware to the level required to definitively demonstrate its sensitivity to bio aerosols or uranium-containing

solids, we did conduct extensive investigations on solutions of NADH and NATA (some of the primary fluorophores in bio materials) and solutions of uranyl nitrate. Based on this work, we have a number of observations and recommendations for further work.

- Frequency-domain (aka phase-sensitive or lock-in detection) techniques are required to achieve sensitive fluorescence measurements with LEDs and laser diodes. Phase-sensitive detection dramatically reduces elastically scattered light and background light from the measured signal. It also dramatically reduces the effect of detector dark noise which is not time-correlated with the fluorescence signal. Finally, the modulation frequency can be optimized to detect target species based on fluorescence lifetime and electronically reject signals from background fluorescent species that might normally cause interference.

- Dispersed fluorescence (i.e. multi-spectral) combined with phase-sensitive detection is likely needed to achieve useful sensitivities for bio and uranium compounds. In the case of bio fluorescence, multi-spectral information will likely be needed to discriminate the bio fluorescence from the background fluorescence which tends to have similar (short) fluorescence lifetime and therefore would not be rejected by phase-sensitive detection alone. For uranium detection, some multi-channel spectral detection would be needed to discriminate it from common background fluorescence.

- Some practical limitations of multi-spectral phase-sensitive detection may be the fact that multiple phase-sensitive detectors would be required. For this LDRD work, we used a commercial single-channel RF lock-in amplifier. To exploit the major advantages of UV LEDs (inexpensive, power efficient, miniature size and weight) to produce a lightweight (possibly hand-held) fluorescence sensor, one would need to develop miniature multi-channel lock-in hardware.

- Our measurements indicate that the sensitivity of the test-bed phase-sensitive fluorimeters are approaching useful levels for bio and uranium. Before committing to design an instrument, further measurements would need to be made on bio aerosols (or solids) to demonstrate the test-bed sensitivity to realistic materials it would be expected to detect. The same is true for uranium detection. In some tests, we conducted with uranium-doped soil targets, for example, we were not able to detect any fluorescence signal.

5. References

1. W. H. Sun, J. P. Zhang, V. Adivarahan, A. Chitnis, M. Shatalov, S. Wu, V. Mandavilli, J. W. Yang and M. A. Khan, Appl. Phys. Lett. **85**, 531 (2004).

2. A. J. Fischer, A. A. Allerman, M. H. Crawford, K. H. A. Bogart, S. R. Lee, R. J. Kaplar, W. W. Chow, S. R. Kurtz, K. W. Fullmer and J. J. Figiel, Appl. Phys. Lett. **84**, 3394 (2004).

3. A. A. Allerman, M. H. Crawford, A. J. Fischer, K. H. A. Bogart, S. R. Lee, D. M. Follstaedt, P. P. Provencio and D. D. Koleske, J. Cryst. Growth **272**, 227 (2004).

4. M. Kneissl, D. W. Treat, M. Teepe, N. Miyashita, N. M. Johnson, Proc. SPIE 5365, 278 (2004).

5. K. Iida, T. Kawashima, A. Miyazaki, H. Kasugai, S. Mishima, A. Honshio, Y. Miyake, M. Iwaya, S. Kamiyama, H. Amano and I. Akasaki, Japan. J. Appl. Phys., 43, L499 (2004).

6. J. Edmond, A. Abare, M. Bergman, J. Bharathn, K. L. Bunker, D. Emerson, K. Haberern, J. Ibbetson, M. Leung, P. Russel and D. Slater, J. Cryst. Growth, 272, 242 (2004).

7. C. G. Van de Walle, C. Sampfl, J. Neugebauer, M. D. McClusky and N. M. Johnson, MRS Internet J. Nitride Semicond. Res. **4S1**, G10.4 (1999).

8. Note that thick, free-standing GaN templates grown by techniques such as hydride vapor phase epitaxy are becoming increasingly available and can demonstrate dislocation densities $< 1x10^{7}$ cm^{-2}. Due to lattice-mismatch issues, these templates are not well suited to use in AlGaN laser structures.

9. S. Nakamura, M. Senoh, S. Nagahama, N. Iwasa, T. Yamada, T. Matsushita, H. Kiyoku, Y. Sugimoto, T. Kozaki, H. Umemoto, M. Sano and K. Chocho, Jpn. J. Appl. Phys., 36, L1568 (1997).

10. K. Doverspike, G. E. Bulman, S. T. Sheppard, T. W. Weeks, M. T. Leonard, H. Kong, H. Dieringer, C. H. Carter, Jr., J. A. Edmond, J. D. Brown, J. T. Swindle, J. F. Schetzina, Y. Song, M. Kuball, and A. V. Nurmikko, Photonics West 1998 Conference.

11. J. R. Lakowicz, *Principles of Fluorescence Spectroscopy*, Third Edition (Springer 2006), Chapters 4 and 5.

12. P. Langer, R. Muller, S. Drost, and T. Werner, Sensors and Acutators B **82**, 1-6 (2002).

13. J. P. deNeufville, A. Kasdan, and R. J. L. Chimenti, Appl. Opt. **20**, 1279-1296 (1981).

14. A. Kasdan, R. J. L. Chimenti, and J. P. deNeufville, Appl. Opt. **20**, 1297-1307 (1981).

15. K. L. Schroder, P. J. Hargis, R. L Schmitt, D. J. Rader, and I. R. Shokair, Proc. SPIE **3855**, 82 (1999).

Distribution

1	MS0123	LDRD office, 1030
1	MS1086	D. L. Barton, 1123
1	MS1086	1123 Department File
5	MS1086	M. H. Crawford, 1123
1	MS1086	M. A. Banas, 1123
1	MS1086	A. M. Armstrong, 1123
3	MS1423	R. Schmitt, 1128
1	MS1423	G. A. Hebner, 1128
1	MS1086	A. A. Allerman, 1126
1	MS1086	J. J. Figiel, 1126
1	MS1086	R. M. Biefeld, 1126
1	MS1085	D. K. Serkland, 1742
1	MS1427	J. M. Phillips, 1100
1	MS0899	Technical Library, 9536 (electronic copy)
1	MS0612	Review & Approval Desk, 9612
1	MS0161	Patent and Licensing Office, 1150


Sandia National Laboratories